Masuda and Uozumi *NPG Asia Materials* (2023) 15:69
https://doi.org/10.1038/s41427-023-00515-7

NPG Asia Materials

ARTICLE Open Access

Highly responsive diabetes and asthma sensors with WO_3 nanoneedle films for the detection of biogases with low concentrations

Yoshitake Masuda[1] and Ayako Uozumi[1]

Abstract

A diabetes sensor was developed to detect low concentrations of acetone gas, which is a diabetes biomarker. A WO_3 nanoneedle film was synthesized via an aqueous process for use as a sensitive sensing membrane. Acetone was adsorbed and oxidized on the WO_3 nanoneedle film, which changed the sensor resistance. The sensor exhibited a high response of $R_a/R_g = 19.72$, where R_a is the sensor resistance in air, and R_g is the sensor resistance in air containing 10 ppmv acetone gas. The sensor also exhibited a high response (25.36) to 1 ppmv NO_2, which is related to asthma. Furthermore, the sensor responded to various biogases associated with diseases. The sensor responses to 10 ppmv of the lung cancer marker gases acetaldehyde and toluene were 13.54 and 9.49, respectively. The sensor responses to 10 ppmv isoprene, ethanol, para-xylene, hydrogen, and NH_3 were 7.93, 6.33, 4.51, 2.08, and 0.90, respectively. Trace amounts of acetone and NO_2 gases (25 and 250 ppbv, respectively) were detected. The limits of detection for acetone and NO_2 gases were estimated to be 2.4 and 1.5 ppbv, respectively. The sensor exhibited superior ability to detect low concentrations of biomarker gases. The unique characteristics of the WO_3 nanoneedle film contributed to its high response rates.

Introduction

Interest in early detection of diseases and chain physical condition are increasing. Diseases induces changes in the components of the body and blood, and biogas components are emitted from the body, such as exhaled breath and skin gases. The correlations between various gases and diseases have been investigated, and disease marker gases have been identified[1–4]. As such, there is strong demand for early detection of diseases by sensing low concentrations of biogases emitted from the living body. Acetone is a marker for diabetes[1–4], and patients with diabetes exhibit acetone skin gas concentrations of 188 ppbv, which is higher than that of a healthy person (87 ppbv)[5]. The acetone concentration in skin gas is correlated with the β-hydroxybutyrate, blood glucose, and HbA1c levels in the blood of diabetic patients. The skin gases from patients with diabetic ketoacidosis have high acetone concentrations (940 ppbv), which decrease to 80 ppbv after insulin therapy. It is expected that early screening will be possible by sensing the acetone concentration in exhaled breath and skin gas with small portable devices such as smartwatches. Nitrogen oxides (NO, NO_2, and HONO) are associated with asthma. NO gas is a marker for asthma, and sensing NO and its oxidation product, NO_2, is useful in patients with asthma[1–4]. Acetaldehyde and toluene[6] are lung cancer markers, and expectations are high for early detection of lung cancer[1–4]. Isoprene is a biomarker produced from intermediates of cholesterol synthesis[1–4]. Ethanol (C_2H_5OH) is a biomarker for alcohol consumption and is detectable in biogas[1–4]. The H_2 concentrations in biogas increase due to overgrowth of intestinal anaerobic bacteria in patients with dyspepsia syndrome[1–4]. Hepatic encephalopathy, congenital enzymatic abnormalities in the urinary tract, *Helicobacter pylori* infection, and other infectious diseases

Correspondence: Yoshitake Masuda (masuda-y@aist.go.jp)
[1]National Institute of Advanced Industrial Science and Technology (AIST), 205, Sakurazaka 4-chome, Moriyama-ku, Nagoya 463-8560, Japan

increase the concentrations of ammonia (NH_3) in the body[1–4]. Additionally, various gases, such as para-xylene, are present in biogas and are useful in determining the state of the body[1–4].

Semiconductor gas sensors exhibit long-term stability, rapid recovery, and heat, ultraviolet, vibration, and chemical resistance. Therefore, they have been used in gas leak detectors. The need for biogas detection has increased in recent years, and semiconductor gas sensors capable of detecting biogas have been developed. In particular, metal oxide nanostructures have attracted considerable attention[7,8] as they are able to detect low-concentrations of gases[9–17]. For example, SnO_2 nanosheets were developed via an aqueous process[18] for use as lung cancer sensors[19,20]. The SnO_2 nanosheets exhibited strong responses to various biogases[21–23]. Psychological stress sensors have been developed from NiO/MnO_2@-NiO[24] and SnO_2 nanosheets[25]. ZnO nanobelts[26] and porous CuO[27] with metal-organic frameworks have been developed to detect low concentrations of biogases. However, new materials and gas sensors are needed to detect low biogas concentrations.

Many semiconductor gas sensors have been developed from SnO_2 or ZnO. However, the sensing properties of WO_3 are expected to differ from those of SnO_2 and ZnO. A WO_3 particulate film-type sensor was synthesized via the sol-gel method, followed by annealing at 500 °C for 2 h in a N_2 atmosphere[28]. The average particle size was 76.77 nm, and the particle size distribution was 20–220 nm. The WO_3 particulate film sensor exhibited responses of 1.1, 1.6, and 20.36 to 5, 10, and 100 ppmv NO_2, respectively, at 200 °C. The detection limit was 5 ppmv NO_2 with a reasonable sensing response of 1.1. The sensor also exhibited a response of 18.51 to 100 ppmv acetone at 200 °C.

A microbrick sensor comprising WO_3 nanosheets was synthesized from a peroxy-tungstic acid (PTA) sol with a hydrothermal method at 180 °C[29]. The widths of the WO_3 microbricks increased from 250–300 to 400–700 nm, and the spacings between them decreased with an increasing quantity of the PTA sol. The thicknesses of the WO_3 films increased from 3.0 to 8.8 μm with an increasing amounts of the PTA sol. The microbrick sensor with WO_3 nanosheets exhibited responses of 1.5, 2.5, and 11.5 to 5, 10, and 100 ppmv NO_2, respectively, at 300 °C. The sensor also exhibited a response of approximately 1 for 100 ppmv acetone.

A WO_3 polycrystalline film sensor was synthesized via direct thermal evaporation of metal tungsten foils in an oxygen atmosphere[30]. The WO_3 film consisted of 800 nm crystals and contained both large and small pores. The WO_3 polycrystalline film-type sensor exhibited responses of 1, 4, and 30 to 1, 10, and 100 ppmv NO_2, respectively, at 250 °C. The sensor was less sensitive to NO and NH_3.

WO_3 thin-film sensors were synthesized with a spray pyrolysis technique, and the film thicknesses were varied[31]. The response (%) was calculated as $100 \times |R_g\text{-}R_a| / R_a$. The sprayed 745 nm-thick WO_3 thin-film-type sensor exhibited responses of 20% ($R_a/R_g = 1.2$) and 97% ($R_a/R_g = 1.97$) to 10 and 100 ppmv NO_2, respectively, at 200 °C. The sprayed WO_3 thin film exhibited a dense dual-scale wire network. The crystallite sizes were estimated to be 69 nm. The detection limit for NO_2 was 10 ppmv. The responses to 100 ppmv H_2S, liquefied petroleum gas, NH_3, CO, and SO_2 gases were 7 ($R_a/R_g = 1.07$), 8 ($R_a/R_g = 1.08$), 9 ($R_a/R_g = 1.09$), 10 ($R_a/R_g = 1.10$), and 12% ($R_a/R_g = 1.12$), respectively.

WO_3 nanoflowers were prepared via a hydrothermal method[32]. The WO_3 nanoflower-type sensor exhibited responses of 10 ($R_a/R_g = 1.1$), 20 ($R_a/R_g = 1.2$), 45 ($R_a/R_g = 1.45$), 105 ($R_a/R_g = 2.05$), 150 ($R_a/R_g = 2.15$), 200 ($R_a/R_g = 3.00$), 210 ($R_a/R_g = 3.10$), and 230% ($R_a/R_g = 3.23$) to 1, 5, 10, 20, 40, 60, 80, and 100 ppmv NO_2, respectively, at 200 °C. The sensor exhibited negligible responses to 100 ppmv CO, H_2S, SO_2, and NH_3.

WO_3 and yttrium-doped WO_3 nanoplates (tungsten:oxygen:yttrium = 22.59:77.20:0.21 at. %) were prepared with a hydrothermal method[33]. The WO_3 nanoplates exhibited responses of 1.36 (36.19%), 1.54 (54.45%), 2.10 (109.86%), and 12.10 (109.8%) to 5, 10, 15, or 20 ppmv NO_2, respectively, at 150 °C. The yttrium-doped WO_3 nanoplates exhibited responses of 3.7 (270%), 21 (1950%), 88 (8722%), and 101 (10022%) to 5, 10, 15, and 20 ppmv NO_2, respectively, at 150 °C.

Bilayer polyaniline-WO_3 (PANI–WO_3) thin films were prepared with a hydrothermal synthesis and in situ chemical oxidative polymerization[34]. The p-type PANI exhibited one-dimensional nanofibers with diameters of approximately 100 nm. The nanofibers were randomly distributed on the surfaces of the n-type flower-like WO_3. p-n junctions were formed between the PANI and WO_3. The bilayer PANI-WO_3 thin-film sensor exhibited responses of 1.18, 1.23, 1.45, 1.66, 2.39, 14.47, and 60.9 to 2, 4, 6, 8, 10, 20, and 30 ppmv NO_2, respectively, at 50 °C.

WO_3 nanorods were synthesized via thermal oxidation[35]. A tungsten film was deposited on an oxidized silicon substrate via sputtering and subsequently subjected to thermal oxidation at 500 °C in air. The tungsten film thickness was 100 nm. The WO_3 nanorods were approximately 80 nm in diameter and 400 nm in length. The WO_3 nanorod-type sensor exhibited responses of 1.50 (50%), 1.80 (80%), 2.115 (115%), 2.65 (165%), and 3.55 (255%) to 2, 5, 10, 20, and 50 ppmv NO_2, respectively, at 225 °C. The WO_3 nanorod-type sensor also exhibited responses of 5, 12, 22, 18, and 19 to 10 ppmv acetone, methanol (CH_3OH), ethanol, H_2S, and NH_3, respectively, at 225 °C.

Acetone gas sensors have also been developed with WO_3. Sea urchin-like WO_3 particles that measured 0.86 μm were prepared with a hydrothermal method at 180 °C[36]. The deep-level emission in the photoluminescence spectra indicated that the particles contained many oxygen vacancies. The sea urchin-like WO_3 sensor exhibited responses of 2.8, 4.7, 6.4, 8.7, 16.9, 27.2, 41.1, 94.1, 144.1, 214.9, and 337.6 to 2, 5, 10, 20, 50, 100, 200, 500, 1000, 2000, and 5000 ppmv acetone, respectively, at 200 °C. The responses to 100 ppmv NO_2, H_2, N,N-dimethylformamide, ethylene glycol ($C_2H_6O_2$), CO, NH_3, CH_3OH, H_2S, and C_2H_5OH were −12, 9, 7, 4, 4, 3, 3, 2, and 2, respectively.

WO_3 nanosheets were prepared with a hydrothermal method at 110 °C and annealed at 350–500 °C[37]. g-C_3N_4 nanosheets were prepared by ultrasonically treating bulk g-C_3N_4. The g-C_3N_4 and WO_3 nanosheets were mixed to form g-C_3N_4-modified WO_3 nanosheets. A 1 wt. % g-C_3N_4-modified WO_3 nanosheet sensor exhibited responses of 3.5, 4.8, 11, 25, 35, and 65 to 0.5, 1, 10, 50, 100, and 1000 ppmv acetone, respectively, at 340 °C. In contrast, the WO_3 nanosheet-type sensor exhibited a response of 12 to 100 ppmv acetone at 340 °C. The addition of g-C_3N_4 to the WO_3 nanosheet sensor enhanced the response of the sensor.

A Cr_2O_3-doped (5 mol%) WO_3 thin-film sensor exhibited responses of 4.19, 6.13, and 8.91 to 10, 15, and 20 ppmv acetone, respectively, at 320 °C[38].

Copper-doped (3 mol%) WO_3 fibers were synthesized via electrospinning[39]. The samples were annealed at 500 °C and quenched to form 3 mol% copper-doped WO_3 hollow fibers. The hollow fibers had wall thicknesses of approximately 300–500 nm. The walls comprised numerous 20–30 nm nanocrystals. The 3 mol% copper-doped WO_3 hollow fiber sensor exhibited a response of 6.43 to 20 ppmv acetone at 300 °C.

Flower-like WO_3 particles composed of intersecting nanoflakes with diameters of 1.5–2 μm were synthesized via a hydrothermal method[40]. The flower-like WO_3 sensor exhibited responses of 12.5 and 10.9 to 100 ppmv C_2H_5OH and acetone, respectively, at 320 °C. Flower-like MoO_3/WO_3 particles with molybdenum:tungsten molar ratios of 4 were also prepared. These particles exhibited responses of 28.5 and 18.2 to 100 ppmv C_2H_5OH and acetone, respectively, at 320 °C. These responses were approximately 2.3- and 1.7-fold higher than those of the flower-like WO_3.

WO_3 particles were prepared with a surfactant-mediated method and annealed at 500 °C[41,42]. Single-crystalline WO_3 plates were prepared via a hydrothermal method with cetyltrimethyl ammonium bromide[42]. The particulate WO_3 gas sensor exhibited responses of 11, 27 to 100, and 1000 ppmv acetone, respectively, at 307 °C[42]. The single-crystalline WO_3 plate-type gas sensor exhibited responses of 15, 105 to 100, and 1000 ppmv acetone, respectively, at 307 °C. The single-crystalline WO_3 plate-type gas sensor also exhibited responses of 10, 19, 5, and 19 to 100 ppmv NH_3, 1000 ppmv NH_3, 100 ppmv alcohol, and 1000 ppmv alcohol, respectively, at 307 °C.

WO_3 hollow spheres with diameters of 400 nm were synthesized in solution via hydrolysis of WCl_6 with carbon microspheres[43]. The WO_3 hollow spheres were annealed at 450 °C for 2 h in air. The shell thicknesses were approximately 30 nm, and the spheres contained holes and wrinkles and were constructed from nanoparticles with diameters of approximately 12 nm. The WO_3 hollow sphere gas sensor exhibited responses of 3.53, 4.56, 6.04, 13.5, 16, 18.6, and 23.1 to 50, 100, 200, 500, 1000, 2000, and 5000 ppmv acetone, respectively, at 400 °C.

WO_3 nanosheets were prepared by deposition from solution and annealed at 300 °C[44]. The surfaces of the nanosheets were modified with silver nanoparticles to form silver quantum dot-sensitized WO_3 nanosheets. The WO_3 nanosheet gas sensor exhibited responses of 2.5, 4.5, 7.5, 9.5, 13, and 14 to 10, 20, 50, 100, 300, and 500 ppmv acetone, respectively, at 340 °C. The silver quantum dot-sensitized WO_3 nanosheet gas sensor exhibited higher responses of 2.5, 5, 8, 12, 17, and 19.5 to 10, 20, 50, 100, 300, and 500 ppmv acetone, respectively, at 340 °C.

WO_3 nanostructures were used as sensors for NO_2 and acetone. However, the responses to low concentrations of gases must be improved for biogas detection. Therefore, WO_3 nanoneedle-derived films were fabricated in this study using an aqueous process. A diabetes sensor was developed with the WO_3 nanoneedle films. The sensor exhibited a high response to 10 ppmv acetone gas, a diabetes marker. The gas sensor responded to acetone and other gases, such as NO_2, acetaldehyde, toluene, isoprene, C_2H_5OH, para-xylene, H_2, and NH_3. The developed semiconductor-type gas sensor was small and lightweight with no size restrictions; therefore, it can be used in small portable devices such as smartwatches.

Experimental

Syntheses of WO_3 and $WO_3(H_2O)_{0.33}$ nanoneedles

Tungstic acid (CAS registration number: 7783-03-1; molecular formula: H_2WO_4; molecular weight: 249.85, FUJIFILM Wako Pure Chemical Corporation, Osaka, Japan), acetonitrile (CAS registration number: 75-05-8; molecular formula: CH_3CN; molecular weight: 41.05, FUJIFILM Wako Pure Chemical Corporation, Osaka, Japan), and hydrochloric acid (CAS registration number: 7647-01-0; molecular formula: HCl; molecular weight: 36.46, FUJIFILM Wako Pure Chemical Corporation, Osaka, Japan) were used as received. Tungstic acid (0.25 mol/L, 120 mL), CH_3CN (10 mL), and HCl (6 mol/L, 5 mL) were dissolved in distilled water (25 mL) and

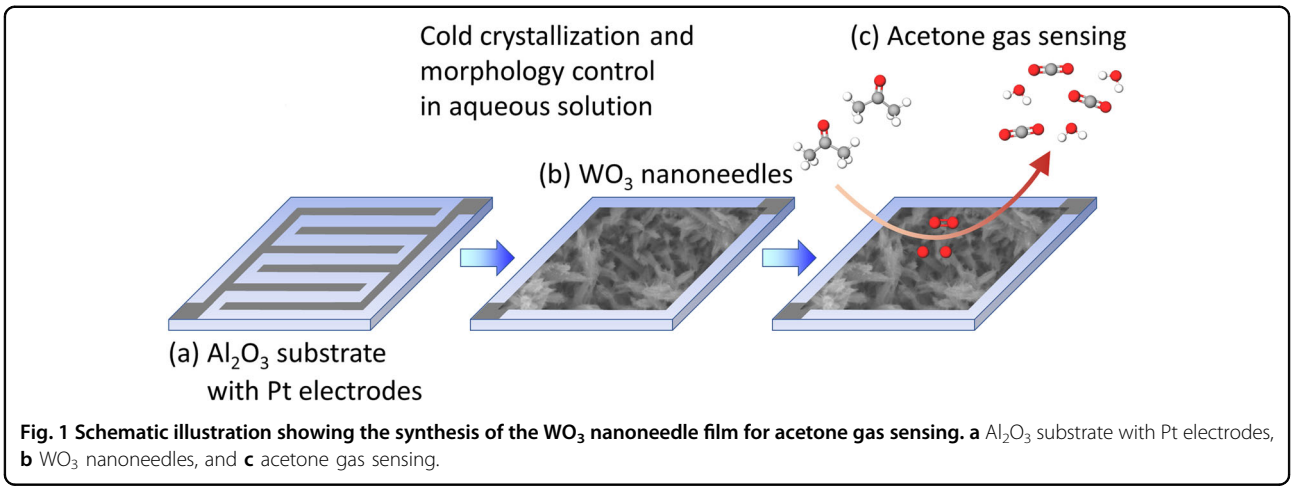

Fig. 1 Schematic illustration showing the synthesis of the WO_3 nanoneedle film for acetone gas sensing. a Al_2O_3 substrate with Pt electrodes, **b** WO_3 nanoneedles, and **c** acetone gas sensing.

maintained at 70 °C for 1 week. The synthesized particles were then removed from the solution by centrifugation and subsequently heated at 300 °C for 2 h in air.

Synthesis of a seed layer for a WO_3 nanoneedle film

Comb-shaped platinum electrodes were formed on an Al_2O_3 substrate (3 mm × 3 mm) via screen printing (Fig. 1a). A platinum heater electrode was deposited on the back surface of the Al_2O_3 substrate. The comb-shaped platinum electrodes were irradiated with vacuum ultraviolet light for 20 min to remove adsorbed organic molecules. Subsequently, the surface became superhydrophilic.

Hydrogen peroxide (30%) (CAS registration number: 722-84-1; molecular formula: H_2O_2; molecular weight: 34.01) with a density of approximately 1.11 g/mL (at a mass fraction of 30%), H_2WO_4 (CAS registration number: 7783-03-1; molecular formula: H_2WO_4; molecular weight: 249.85), and polyvinyl alcohol (PVA; CAS registration number: 9002-89-5; molecular formula: $(-CH_2CHOH-)_n$; average degree of polymerization: 1500 or more (1500–1800) were used as received.

Tungstic acid (1.25 g) and PVA (0.5 g) were dissolved in H_2O_2/water (30%) (10 mL). The Al_2O_3 substrate was coated with a tungstic acid solution via dip-coating. The substrate was heated at 500 °C for 2 h in air to form a seed layer.

Synthesis of a WO_3 nanoneedle film gas sensor

Tungstic acid (0.25 mol/L, 120 mL), CH_3CN (10 mL) and HCl (6 mol/L, 5 mL) were dissolved in distilled water (25 mL). The substrate with the seed layer was immersed in the solution and maintained at 70 °C for 7 d to form a WO_3 nanoneedle film (Fig. 1b). The substrate was immersed face-down to suppress precipitation of the particles generated in the solution onto the substrate.

Characterization of the WO_3 nanoneedle film

The crystal structures of the synthesized WO_3 nanoneedles and WO_3 nanoneedle film were evaluated with X-ray diffractometry (XRD; SmartLab, Rigaku Co. Ltd., Japan) operating at 40 kV and 30 mA with Cu Kα radiation ($\lambda = 1.5418$ Å). The morphologies of the WO_3 nanoneedles and sensor structures were observed with field emission scanning electron microscopy (FE-SEM; JSM-6335FM, JEOL, Japan).

The samples were also examined with transmission electron microscopy (TEM; Tecnai Osiris, 200 kV, FEI), high-angle annular dark-field scanning TEM (HAADF-STEM), energy-dispersive X-ray spectroscopy (EDS; JED-2300T, DRY SD100GV, JEOL Ltd.), and electron energy-loss spectroscopy (Quantum ER, Gatan, Inc.). Cross-sectional samples were prepared with a focused ion beam (10–40 kV). The WO_3 nanoneedle film was fixed with a resin for cross-sectional observations. Some of the WO_3 nanoneedle films embedded in the resin were peeled off the Al_2O_3 substrate during cross-sectioning via ion milling.

Evaluation of the gas sensing performance

An Al_2O_3 substrate with a WO_3 nanoneedle film was evaluated as a gas sensor (Fig. 1c). The sensor was heated to 300 °C wit a platinum heater on the back side of the sensor. The resistance of the sensor in air (R_a) was evaluated with a small resistance-measuring instrument under a dry air flow (N_2:$O_2 = 80$:20). Because of the measurement range of the resistance meter, the noise in the measurement data was high at resistance values ≥ 1 MΩ. N_2 and O_2 gases in gas cylinders (G1 grade, > 99.99995 vol. % and G1 grade, > 99.99995 vol.%, respectively) were used for the evaluations. The resistance of the sensor to target gases (R_g) was evaluated by measuring the resistance under flowing dry air (N_2:$O_2 = 80$:20) containing 10 ppmv of the target gas. Acetone, H_2, NH_3, NO_2, C_2H_5OH,

toluene, acetaldehyde, para-xylene, and isoprene were used as the target gases. The total flow rate was 100 cm^3 min^{-1}. The sensor response (R_a/R_g) was calculated from the sensor resistance in air (R_a) and sensor resistance in air containing the target gas (R_g).

The 50% (T50 (res)) and 90% response times (T90 (res)) are the times needed for the sensor resistance to achieve 50 and 90%, respectively, of the total resistance change resulting from exposure to the target gas, and there were calculated using:

$$T50(\mathrm{res}) : R_a - \Delta R \times 0.5 \quad (1)$$

$$T90(\mathrm{res}) : R_a - \Delta R \times 0.9 \quad (2)$$

$$\Delta R = R_a - R_g \quad (3)$$

where the 50% (T50 (rec)) and 90% recovery times (T90 (rec)) are the times needed for the sensor resistance to reach 50 and 90%, respectively, of the total resistance change upon exposure to the target gas and were calculated as:

$$T50(\mathrm{rec}) : R_g + \Delta R \times 0.5 \quad (4)$$

$$T90(\mathrm{rec}) : R_g + \Delta R \times 0.9 \quad (5)$$

$$\Delta R = R_a - R_g \quad (6)$$

The resistance in NO_2 gas was higher than that in air because NO_2 is an oxidizing gas. The sensor response was calculated from R_g/R_a. The 50% (T50 (res)) and 90% response times (T90 (res)) were defined as:

$$T50(\mathrm{res}) : R_a + \Delta R \times 0.5 \quad (7)$$

$$T90(\mathrm{res}) : R_a + \Delta R \times 0.9 \quad (8)$$

$$\Delta R = R_g - R_a \quad (9)$$

The 50% (T50 (rec)) and 90% recovery times (T90 (rec)) were defined as:

$$T50(\mathrm{rec}) : R_g - \Delta R \times 0.5 \quad (10)$$

$$T90(rec) : R_g - \Delta R \times 0.9 \quad (11)$$

$$\Delta R = R_g - R_a \quad (12)$$

The concentrations of the gases produced in this study are displayed in parts per million by volume (ppmv), parts per billion by volume (ppbv), and parts per trillion by volume (pptv). The concentrations of the gases produced in this study, namely, 1 ppmv, 1 ppbv, and 1 pptv, were equivalent to 1 μmol/mol, 1 nmol/mol, and 1 pmol/mol, respectively. Parts per million by volume (ppmv, μmol/mol) was used for the volume fractions, and parts per million weight (ppmw) were used for the mass fractions. In several gas sensor studies, 1 ppmv, 1 ppbv, and 1 pptv were referred to as 1 ppm, 1 ppb, and 1 ppt, respectively.

The sensing evaluations presented in Section "Low-concentration gas sensing and limit of detection (LOD) for the WO_3 nanoneedle filmsensor" for low gas concentrations were conducted precisely and compared with the simple evaluations described in Section "Gas sensing performance and gas selectivity of the WO_3 nanoneedle film sensor". Trace amounts of the reducing gas were adsorbed by the evaluation system, which decreased the responses to NO_2 in the evaluations described in Section "Gas sensing performance and gas selectivity of the WO_3 nanoneedle film sensor".

Results and discussion

Syntheses of WO_3 and $WO_3(H_2O)_{0.33}$ nanoneedles

Nanoneedles were crystallized from an aqueous solution containing tungstic acid (0.25 mol/L, 120 mL), CH_3CN (10 mL), HCl (6 mol/L, 5 mL), and water (25 mL) and were maintained at 70 °C for 1 week (Fig. 2a). The nanoneedles were approximately 100 nm long and 10 nm wide. The aspect ratio was approximately 10 (100 nm/10 nm). Their structures and sizes were maintained after annealing at 300 °C for 2 h in air (Fig. 2b). The X-ray diffraction (XRD) pattern for the as-synthesized nanoneedles was assigned to $WO_3(H_2O)_{0.33}$ (Powder Diffraction Data File (PDF) No. 01-087-1203) (Fig. 3a). The nanoneedles underwent a phase transformation into WO_3 (PDF No. 01-085-2459) while annealing at 300 °C for 2 h in air (Fig. 3b). The XRD pattern for WO_3 was similar to that of $WO_3(H_2O)_{0.33}$. The diffraction peak at 18°, which was observed for $WO_3(H_2O)_{0.33}$ but not for WO_3, was characteristic of $WO_3(H_2O)_{0.33}$ and was attributed to the {111} plane of $WO_3(H_2O)_{0.33}$. This peak was useful for distinguishing $WO_3(H_2O)_{0.33}$ and WO_3. The slight residual $WO_3(H_2O)_{0.33}$ was completely transformed into WO_3 by extending the annealing period.

Synthesis of a WO_3 nanoneedle film for use in a gas sensor

A WO_3 nanoneedle film was formed on the Al_2O_3 substrate via a seed layer in an aqueous solution containing tungstic acid (0.25 mol/L, 120 mL), CH_3CN (10 mL), HCl (6 mol/L, 5 mL), and distilled water (25 mL) at 70 °C for 7 d (Fig. 4a). The substrate was uniformly covered with WO_3 nanoneedles, which were elliptical with tips (Fig. 4c1–d2). The nanoneedles were approximately 500 nm long and 5–50 nm wide (Fig. 4c2, d2). The

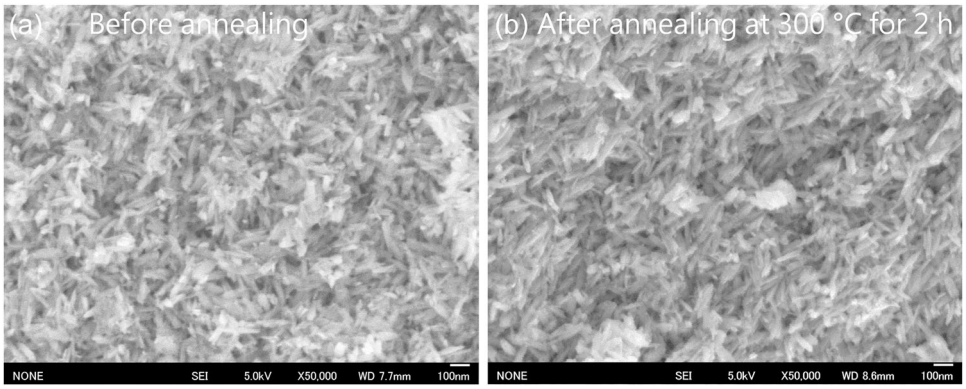

Fig. 2 SEM images of the WO_3 $(H_2O)_{0.33}$ nanoneedles. a The WO_3 $(H_2O)_{0.33}$ nanoneedles before annealing at 300 °C for 2 h in air. **b** The WO_3 $(H_2O)_{0.33}$ nanoneedles after annealing at 300 °C for 2 h in air.

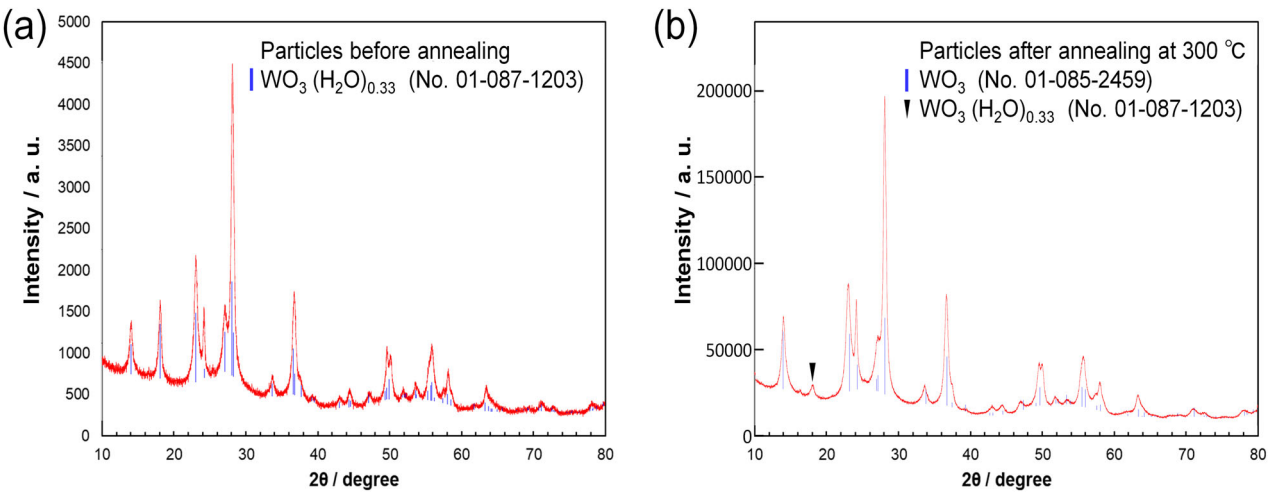

Fig. 3 XRD patterns for the WO_3 $(H_2O)_{0.33}$ nanoneedles. a The $WO_3(H_2O)_{0.33}$ nanoneedles before annealing at 300 °C for 2 h in air. **b** The WO_3 nanoneedles after annealing at 300 °C for 2 h in air.

aspect ratios were approximately 10 (500 nm/50 nm). Smaller nanobranches grew from the nanoneedles via dendritic crystal growth. The angles between the nanoneedles and nanobranches were approximately 90°, as shown in Fig. 4d2. The WO_3 crystals were hexagonal. Considering the shapes and branching angles, the longitudinal direction of the nanoneedles may be along the c-axis of WO_3, and the longitudinal direction of the nanobranches may be perpendicular to the c-axis of WO_3. The nanoneedle structures were maintained during annealing at 300 °C for 2 h in air (Fig. 4b).

Cross-sectional images of the WO_3 nanoneedle film on the Al_2O_3 substrate show that the Al_2O_3 substrate was covered with a dense particle layer and that WO_3 nanoneedles were formed on the dense particle layer (Fig. 5a–b). Because the Al_2O_3 substrate was a sintered body of Al_2O_3 particles, the surface exhibited irregularities measuring several micrometers. In general, it is difficult to form a uniform film on a substrate with an unevenness of several micrometers. However, in this study, a dense particle layer and WO_3 nanoneedle film were formed along an uneven substrate.

The XRD pattern of the WO_3 nanoneedle film was assigned to WO_3 (PDF No. 01-085-2459) (Fig. 6a). A small $WO_3(H_2O)_{0.33}$ peak (PDF No. 01-087-1203) was observed at 18°. The diffraction peaks of Al_2O_3 and platinum were also detected because the Al_2O_3 substrate contained comb-shaped platinum electrodes on its surface. The WO_3 nanoneedle film was composed of a single phase of WO_3 (PDF No. 01-085-2459) after the annealing treatment at 300 °C for 2 h in air (Fig. 6b). Annealing completely transformed the small amount of the $WO_3(H_2O)_{0.33}$ phase into WO_3.

The morphologies of the dense particle layers and WO_3 nanoneedle films were observed with TEM (Fig. 7a). The

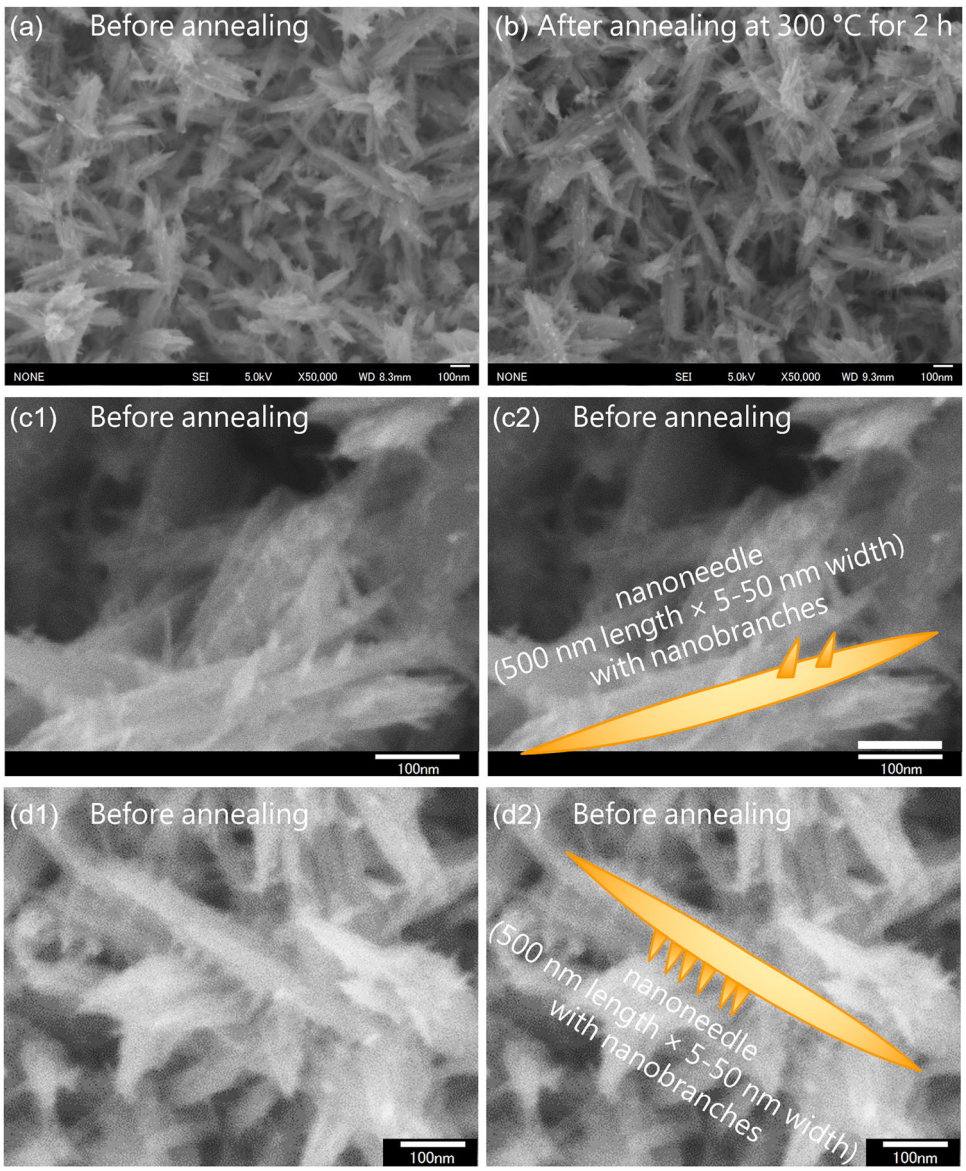

Fig. 4 SEM images of the WO_3 nanoneedle film. a The WO_3 nanoneedle film before annealing at 300 °C for 2 h in air. **b** The WO_3 nanoneedle film after annealing at 300 °C for 2 h in air. (**c1**, **d1**) Magnified images of **a**. **c2** Image in (**c1**) with a WO_3 nanoneedle illustrated to show its size and morphology. **d2** Image in (**d1**) with a WO_3 nanoneedle illustrated to show its size and morphology.

dense particle layer was composed of spherical particles. The WO_3 nanoneedles were elliptical with tips similar to those observed with FE-SEM. The nanoneedles were approximately 500 nm long and 5–50 nm wide. Moreover, smaller nanoneedles were observed with approximate 10–100 nm lengths and 5–10 nm widths. The lattice spaces were calculated from the selected-area electron diffraction (SAED) patterns of the nanoneedles (Fig. 7b). The lattice spacings of 0.316, 0.317, 0.381, 0.364, and 0.628 nm were assigned to the {020}, {020}, {001}, {001}, and {010} planes of WO_3, respectively. Additionally, a weak diffraction pattern was observed. The calculated lattice spacing was 0.480 nm. This peak was assigned to the {111} plane of $WO_3(H_2O)_{0.33}$. The main phase of the nanoneedles was WO_3 and included a small amount of $WO_3(H_2O)_{0.33}$, which was consistent with the XRD pattern of the WO_3 nanoneedle film.

The magnified cross-sectional TEM image in Fig. 8a shows that a dense particle layer was formed along the uneven surfaces of the Al_2O_3 substrate, indicating that the WO_3 nanoneedle film was formed on the dense particle layer.

HAADF-STEM images provide contrast based on factors that affect electron scattering, such as the sample

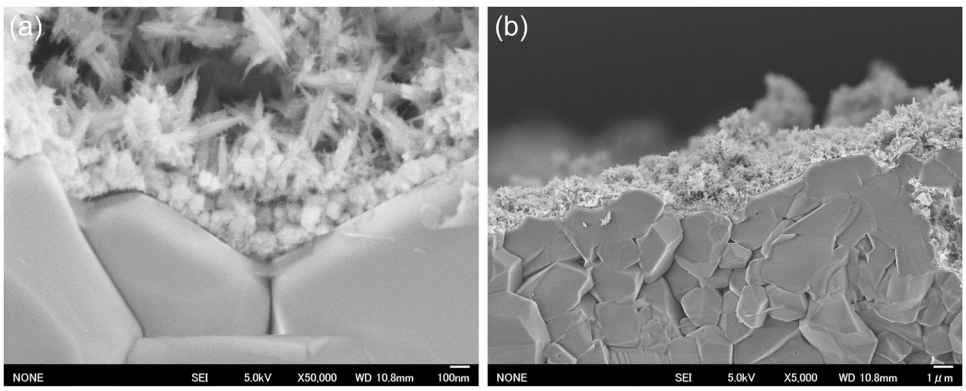

Fig. 5 Cross-sectional image of WO_3 nanoneedle films. Cross-sectional image of **a** WO_3 nanoneedle film on the Al_2O_3 substrate. **b** A low magnification image of (**a**).

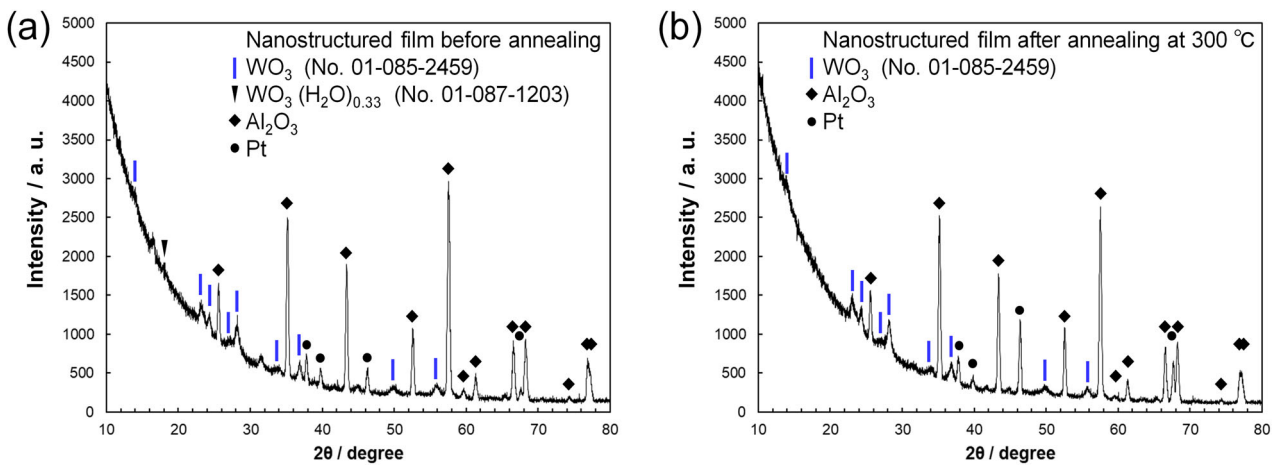

Fig. 6 XRD patterns of the WO_3 nanoneedle films. a The WO_3 nanoneedle film before annealing at 300 °C for 2 h in air. **b** The WO_3 nanoneedle film after annealing at 300 °C for 2 h in air.

density, sample thickness, and composition (atomic number) (Fig. 8b). Detailed morphologies of the dense particle layer and WO_3 nanoneedle film were observed. Tungsten was detected in both the dense particle layer and the WO_3 nanoneedle film in the EDS maps (Fig. 8c). The dense particle layer was composed of WO_3 particles. Aluminum was uniformly distributed on the Al_2O_3 substrate. A clear interface was observed between the dense particle layer and the Al_2O_3 substrate. No reactions occurred between the WO_3 and Al_2O_3.

The WO_3 nanoneedles were examined with high-resolution images, which showed that they had one-dimensional shapes (Fig. 9a). The nanoneedles exhibited lattice fringes perpendicular to their long directions (Fig. 9b). The magnified image clearly shows the lattice spaces of the {001} plane of WO_3 (Fig. 9c), which were perpendicular to the long directions of the nanoneedles. The distance between the yellow lines, which were the lattice spaces for {001} WO_3, was 0.38 nm. The fast Fourier transform (FFT) image in Fig. 9d shows clusters of white dots at the 1 and 7 o'clock positions. A lattice spacing of 0.380 nm was calculated from the FFT image, which was assigned to the {001} plane of WO_3. This indicated that the long direction of the WO_3 nanoneedles was arrayed in the stacking direction of the {001} planes of WO_3. That is, the long direction of the WO_3 nanoneedles was along the <001> direction, which was the c-axis of WO_3.

The lengths of the nanobranches were calculated as follows. The long direction of the WO_3 nanoneedles in the TEM image shown in Fig. 10a was the 4 o'clock direction. The magnified image showed a clear lattice fringe (Fig. 10b). The FFT image showed white spots at the 1 o'clock position, perpendicular to the lengths of the WO_3 nanoneedles (Fig. 10c). A lattice spacing of 0.637 nm was calculated from the FFT image, which was assigned to

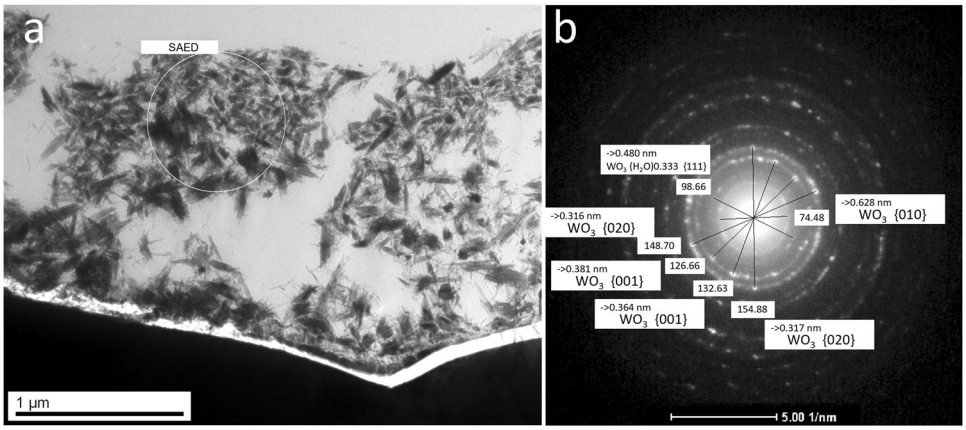

Fig. 7 TEM analysis of the WO_3 nanoneedles. a TEM image of the WO_3 nanoneedle film. **b** SAED pattern for the WO_3 nanoneedles.

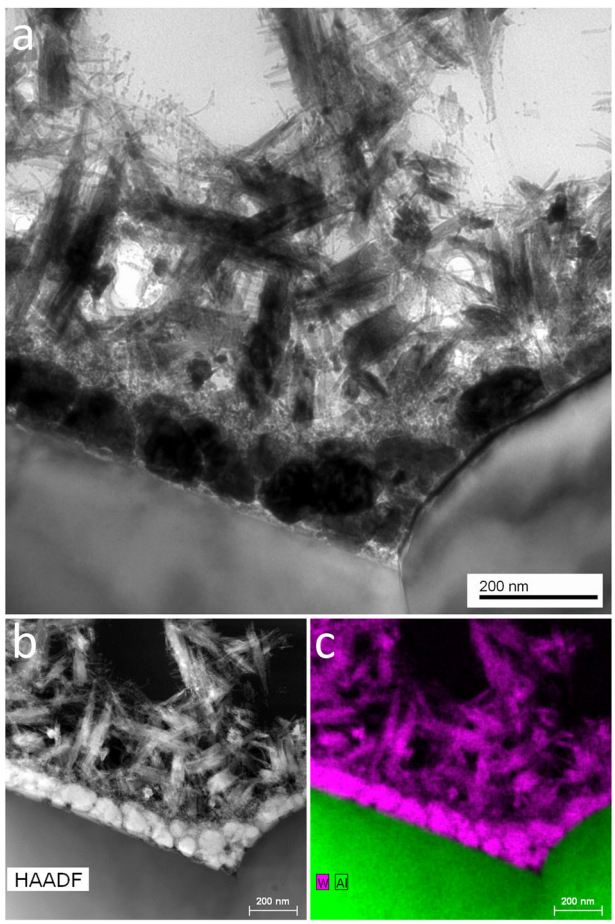

Fig. 8 TEM analysis of the WO_3 nanoneedles. a Magnified cross-sectional TEM image of the WO_3 nanoneedle. **b** HAADF-STEM image of the WO_3-nanoneedle film. **c** EDS maps for tungsten and aluminum on the WO_3 nanoneedle film.

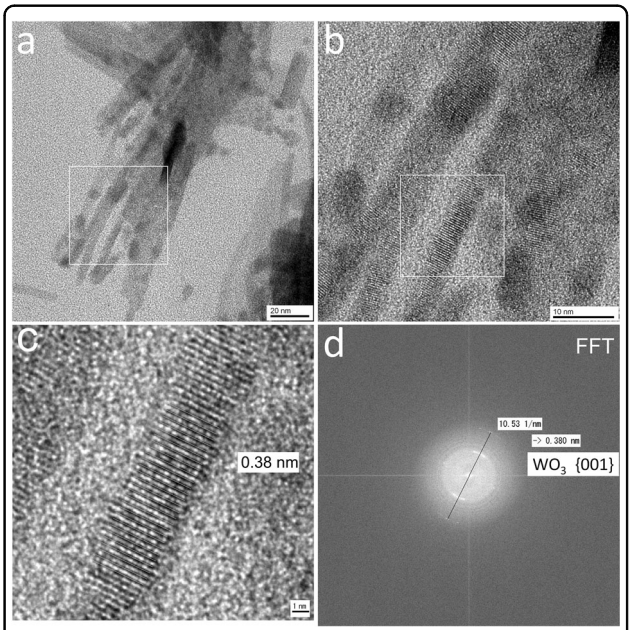

Fig. 9 High-resolution TEM analysis of the WO_3 nanoneedles. High-resolution TEM image of **a** the WO_3 nanoneedles, **b** Magnified image of the demarcated area in (**a**). **c** Magnified image of the demarcated area in (**b**) showing the lattice spaces of the {001} plane of WO_3. **d** FFT image of (**b**) showing the lattice spaces of the {001} plane of WO_3.

the {010} plane of WO_3. This indicated that the direction perpendicular to the length of the WO_3 nanoneedles was <010>. The long direction of the WO_3 nanoneedle was <001>, which was the c-axis, whereas the long direction of the nanoneedle branches was <010>. The angle between the long direction of the WO_3 nanoneedles and the long direction of the nanobranches was 90°. This is consistent

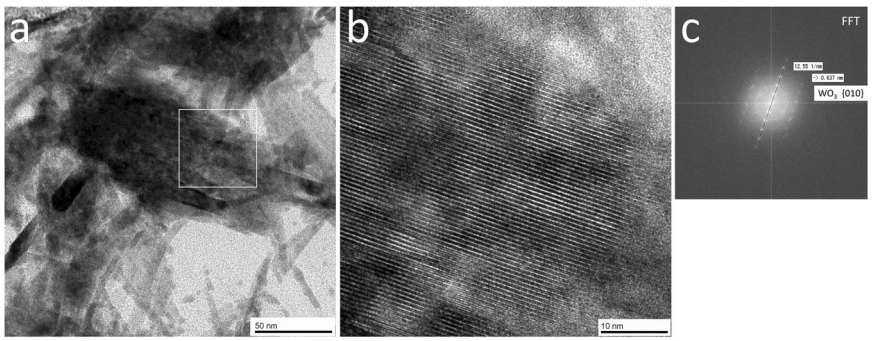

Fig. 10 High-resolution TEM analysis of the WO_3 nanoneedles. a High-resolution TEM image of the WO_3 nanoneedles. **b** Magnified image of the demarcated area in (**a**). **c** FFT image of (**b**) showing the lattice spaces of the {010} plane of WO_3.

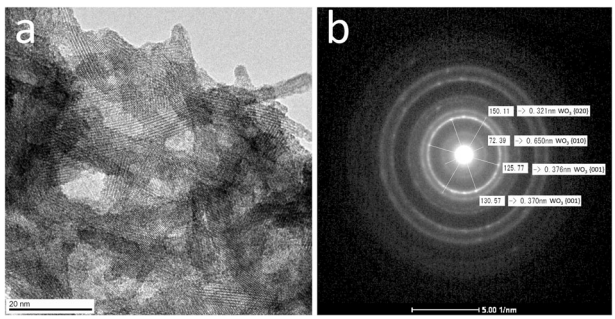

Fig. 11 High-resolution TEM image and FFT image of the WO_3 nanoneedles. a High-resolution TEM image of the WO_3 nanoneedles. **b** FFT image of (**a**) showing the lattice spaces of WO_3.

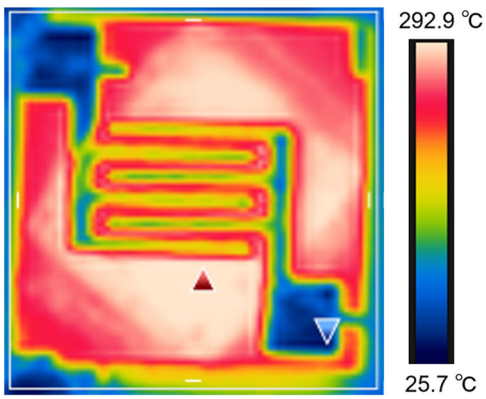

Fig. 12 Thermal image ofthe WO_3 nanoneedle. Thermal image of the WO_3 nanoneedle film on the Al_2O_3 substrate with a platinum heater.

with the FE-SEM observations (Fig. 4d2) and the hexagonal crystal structure of WO_3.

The growth direction of the WO_3 nanoneedles was also evaluated. The WO_3 nanoneedles exhibited clear lattice fringes (Fig. 11a). The lattice spaces were calculated from the strong rings in the FFT images (Fig. 11b). The lattice spacings of 0.370, 0.376, 0.650, and 0.321 nm were assigned to the {001}, {001}, {010}, and {020} planes of WO_3, respectively. The <001> and <010> directions represented the long directions of the WO_3 nanoneedles and nanobranches, respectively. This was also consistent with our hypothesis regarding the growth directions and connection angles of the WO_3 nanoneedles and nanoneedle branches.

Gas sensing performance and gas selectivity of the WO_3 nanoneedle film sensor

A WO_3 nanoneedle film was formed on an Al_2O_3 substrate for use as a gas sensor. The gas sensor was heated to 300 °C with a platinum heater (Fig. 12). Heating of the gas sensor improved its response and response and recovery times.

The gas sensor exhibited a resistance in air of $R_a = 2.02$ MΩ. The resistance decreased significantly to $R_g = 0.10$ MΩ in 10 ppmv acetone gas (Fig. 13a). The gas sensor exhibited a high response of $R_a/R_g = 19.72$ (Fig. 14). The gas sensor exhibited a fast response to acetone with T50 (res) <5 s and T90 (res) <5 s. The gas sensor also exhibited fast recoveries of T50 (rec) = 595 s and T90 (rec) = 2355 s. This gas sensor could be used to detect acetone, a marker gas for diabetes.

The gas sensor exhibited high responses to various biogases. The sensor responses to acetaldehyde, toluene, isoprene, C_2H_5OH, para-xylene, and H_2 were 13.54, 9.49, 7.93, 6.33, 4.51, and 2.08, respectively (Fig. 14). Additionally, the gas sensor exhibited a high response to NO_2, which is an oxidizing gas; R_g was within the detection range. The response rates for NO_2 were 40–10 ppmv. Considering the width of the noise, the response may be several times greater than that at 40. In contrast, a low sensor response of 0.90 was obtained for NH_3. This indicated that acetaldehyde, toluene, isoprene, C_2H_5OH, para-xylene, H_2, and NO_2 was detected without the influence of coexisting NH_3 gas.

The gas sensor exhibited fast responses (T50 (res) < 5 s and T90 (res) < 5 s) to C_2H_5OH, H_2, and NO_2. The gas

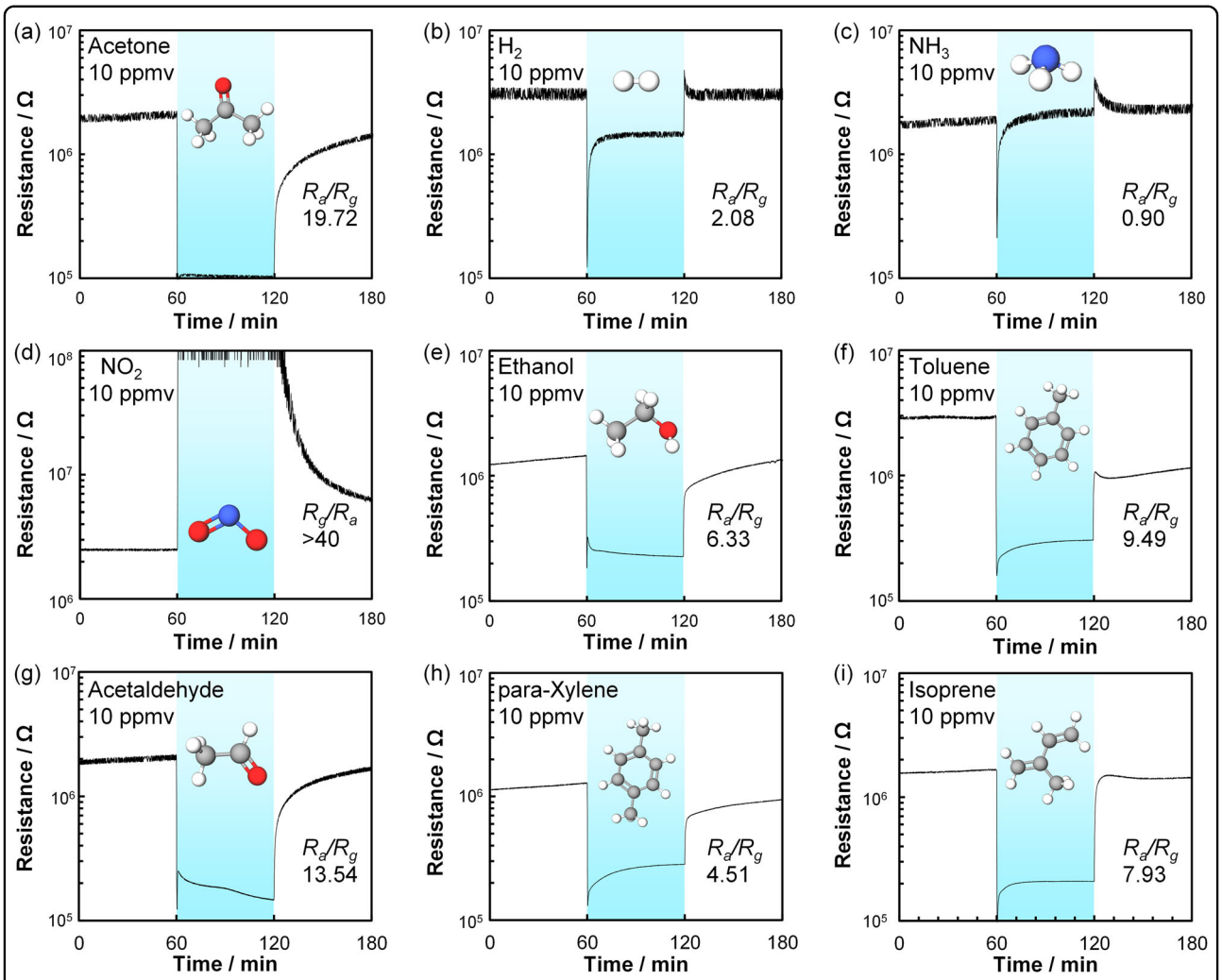

Fig. 13 Electrical resistances at 300 °C for 10 ppmv gases. a Acetone, **b** H_2, **c** NH_3, **d** NO_2, **e** C_2H_5OH, **f** Toluene, **g** Acetaldehyde, **h** para-xylene, and **i** isoprene.

sensor exhibited fast responses (T50 (res) < 5 s and T90 (res) < 10 s) to acetaldehyde, toluene, isoprene, and paraxylene. The gas sensor exhibited fast recoveries (T50 (rec) < 10 s and T90 (rec) < 10 s) for H_2 and NO_2. The T50 (rec)/T90 (rec) recovery times for toluene, isoprene, para-xylene, C_2H_5OH, and acetaldehyde were 10 s/50 s, 35 s/145 s, 50 s/1990 s, 115 s/2210 s, and 410 s/2390 s, respectively.

High and fast sensor responses to various biogases were obtained due to the nano/microstructures of the WO_3 nanoneedle films. Numerous spaces were formed between the WO_3 nanoneedles, as shown in the TEM image in Fig. 8a. Sensors for detecting low gas concentrations require a large surface areas and a gas flow paths for the diffusion of gas molecules. The spaces in the WO_3 nanoneedle film led to large surface areas and provided gas flow paths for sensing gases with low concentrations. Additionally, the WO_3 nanoneedles contained nanobranches, which increased the surface area and number of adsorption sites for gas molecules. The WO_3 nanoneedles exhibited high electrical conductivity in the longitudinal direction owing to the absence of grain boundaries. Shape anisotropy and high electrical conductivity are beneficial for gas sensors that detect changes in resistance.

The nano/microstructure of the sensitive membrane in a gas sensor requires a high surface area, porosity, gas flow paths, and a suitable thickness and conductivity. In particular, gas molecules should flow to reach the interface between the sensitive membrane and substrate to provide high responses to low gas concentrations. The sensitive membrane should be porous to form flow paths for the gas molecules because they cannot flow through a dense membrane. Additionally, the membrane should be thin to ensure that the gas molecules reach the interface between the sensitive membrane and the substrate to obtain a strong sensor response. Thick and porous films are

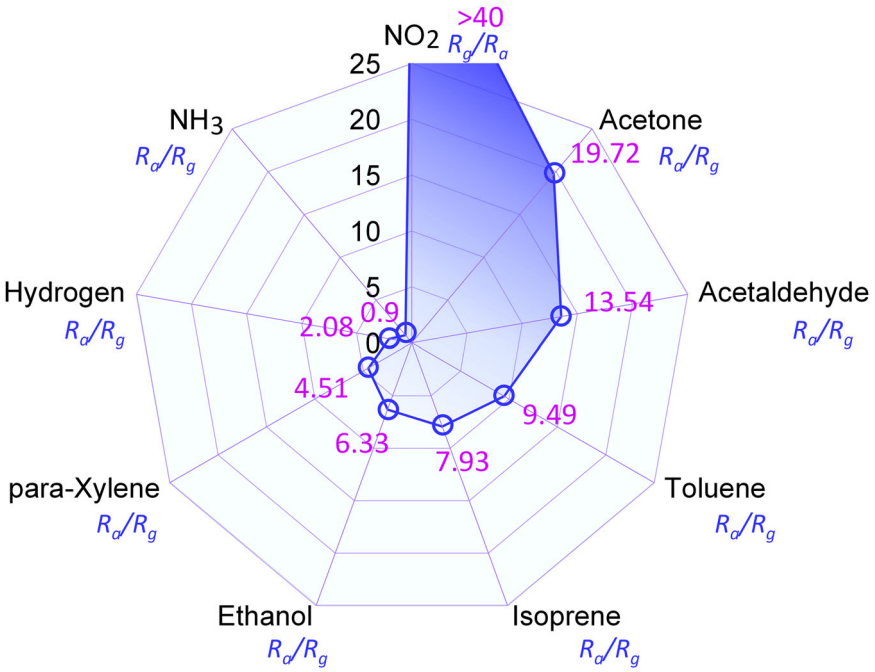

Fig. 14 Sensor signal responses. Sensor signal responses to 10 ppmv NO_2, acetone, acetaldehyde, toluene, isoprene, C_2H_5OH, para-xylene, H_2, and NH_3.

effective in detecting high gas concentrations because many molecules react with them. Thin and porous films are effective for detecting gases with low concentrations. Low-concentration gases react only on the surface of the thick porous film because of the small number of molecules. Only the surface of a thick, porous film contributes to the change in resistance. The internal areas of thick, porous films do not react with the gas and therefore do not contribute to the resistance change. Because the resistance changes only on the surface of the thick, porous film, the resistance change in the sensor element is small. Therefore, thick, porous films are unsuitable for detecting gases with low concentrations. However, almost all of a thin porous film contributes to the resistance change. Therefore, thin, porous films exhibit high sensor responses to low gas concentrations. The optimum film thickness depends on the gas concentration and porosity of the sensitive film. The molecular weight, adsorption capacity, oxidation reactions, and material properties of the sensitive film also determine the optimal film thickness.

Furthermore, the resistance of the sensor must be within the measurable ranges of small resistance meters. However, thin, porous films generally exhibit high resistances that cannot be measured with small resistance meters. In this study, the resistance of a thin, porous membrane was controlled to within the measurement range with the high electrical conductivity in the longitudinal directions of the WO_3 nanoneedles. The WO_3 nanoneedle film was effective in measuring low-concentration gases.

Low-concentration gas sensing and limit of detection (LOD) for the WO_3 nanoneedle film sensor

The sensor responses increased in the order 10 ppmv NO_2, acetone, acetaldehyde, toluene, isoprene, C_2H_5OH, para-xylene, H_2, and NH_3 (Fig. 14). In particular, the sensor exhibited strong responses to NO_2 and acetone. The performance of the sensor was evaluated with low concentrations of NO_2 and acetone.

The sensor exhibited responses of 1.049, 1.218, 1.491, 2.043, 2.392, 3.591, 5.713, 6.777, 7.418, and 7.656 to 25, 50, 75, 100, 125, 250, 500, 750, 1000, and 1250 ppbv acetone gas, respectively (Fig. 15a, b). The approximate straight line calculated over the range 25–125 ppbv is represented in Eq. 13 (Fig. 15c).

$$y = 14.044x - 0.5855 \quad (13)$$

The LOD is a key figure of merit in trace analyses. The analytical signal is clearly differentiated from noise at the LOD concentration. According to the IUPAC definition, the LOD of a sensor is the concentration at which the noise level is less than one-third of the signal level[45]. The theoretical LOD can be calculated with Eq. (14)[45]. The LOD is the analyte concentration that produces a

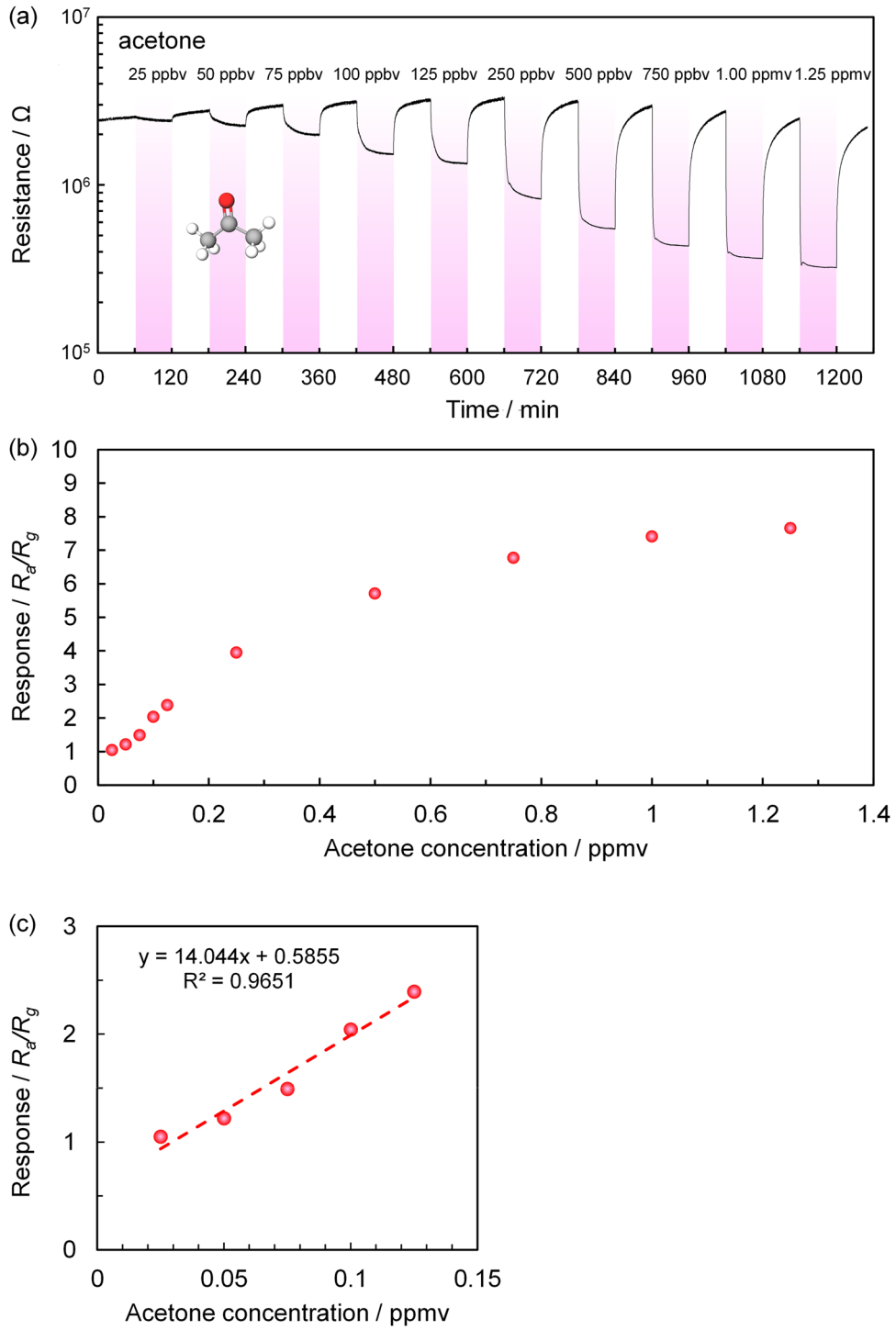

Fig. 15 Sensing performance for acetone gas. a Electrical resistances to 25–1.25 ppmv acetone at 300 °C. **b** Responses to 25–1.25 ppmv acetone. **c** Responses to 25–125 ppbv acetone.

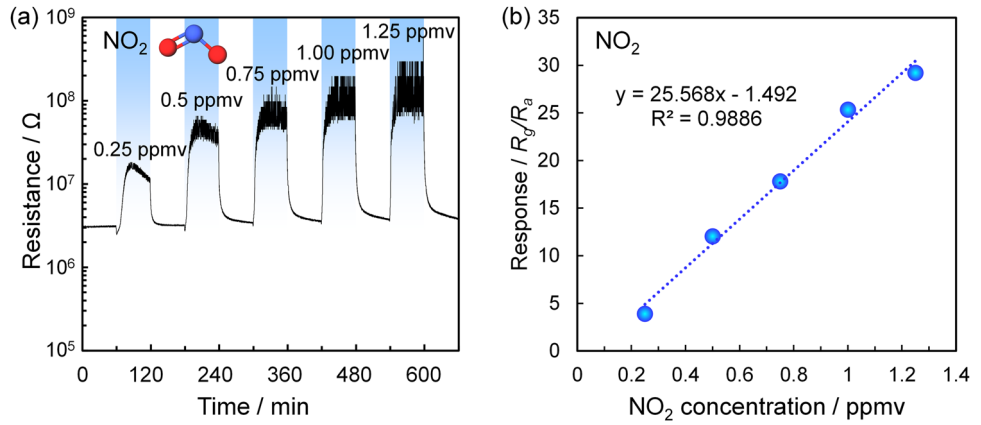

Fig. 16 Sensing performance for NO_2. **a** Electrical resistances for 250–1.25 ppmv NO_2 at 300 °C. **b** Response to 250–1.25 ppmv NO_2.

response that is threefold higher than the noise level of the device[45].

$$\mathrm{LOD} = 3 \times \mathrm{RMS}/\mathrm{S} \tag{14}$$

where RMS is the standard root-mean-square deviation of the device noise and S is the analytical sensitivity. The RMS value of the sensor resistance in air was calculated from 100 data points.

An LOD of 2.4 ppbv was estimated for acetone gas from an RMS of 0.01106 and S of 14.044. Acetone is a well-known diabetes marker. There is a strong demand in the health care field for gas sensors that can monitor trace amounts of acetone in the exhaled breath and skin gases. The WO_3 nanoneedle sensor film can be used to detect low concentrations of acetone in skin gas and to distinguish the acetone levels of patients with diabetes (188 ppbv) from that of healthy individuals (87 ppb)v[5]. This sensor exhibited detection of trace amounts of acetone in health care applications.

The sensing capabilities were evaluated with trace amounts of NO_2. The sensor responses were 3.93, 12.06, 17.83, 25.36, and 29.24 to 0.25, 0.5, 0.75, 1, and 1.25 ppmv NO_2 gas (Fig. 16a). The approximate straight line calculated over the range 0.25–1.25 ppmv is shown in Eq. 15 (Fig. 16b).

$$y = 25.568x - 1.492 \tag{15}$$

An LOD of 1.5 ppbv was estimated from an RMS of 0.01291 and S of 25.568 for NO_2 gas. This indicated that the sensor detected low concentrations of NO_2 gas. The sensor can be used to sense low concentrations of NO_2 gas in biogases, such as in exhaled breath and skin gases, as well as gases in living and mobile spaces. NO_2 is dangerous, and there is a need to detect minute amounts. Additionally, the detection of NO_2 gas is useful in monitoring asthma because NO is a marker for asthma and is easily oxidized to NO_2 gas.

Comparison of the sensing performance for NO_2 or acetone

Various WO_3 nanostructures have been developed for sensing NO_2 (Table 1)[28–35] or acetone (Table 2)[36–40,42–44]. The WO_3 nanostructures exhibited high performance in the detection of low-concentration gases. Moreover, the WO_3 nanoneedle film exhibited responses of 25.36 and 7.418 to 1 ppmv NO_2 and acetone, respectively. The WO_3 nanoneedle film exhibited a higher response than previously reported films.

The concentrations of NO_2 (Table 1) or acetone (Table 2) differed in each study. The responses (R_a/R_g) for each sensor to 0 ppmv NO_2 and acetone were 1, indicating no response. The responses to 1 ppmv NO_2 and acetone gas were calculated for simple comparison. For a more accurate comparison, the responses were compared for the same gas concentration. Additionally, it was necessary to perform evaluations with the same measuring device. Measurement method standardization is also required for gas sensors used in detecting low gas concentrations.

Sensing mechanism for the WO_3 nanoneedle film sensor

In air, oxygen is adsorbed on the surfaces of n-type semiconductor particles such as WO_3, SnO_2, or ZnO. Electrons in the n-type semiconductors are transferred to the adsorbed oxygen atoms, and an electron depletion layer is formed on the surfaces of the particles. The electron depletion layer has a low electron density and electrical conductivity. The electrical resistance of the particulate film increases due to formation of the electron-depletion layer at the grain boundaries. For combustible gases such as volatile organic compounds, the combustible gas molecules and adsorbed oxygen on the particle surface undergo oxidation

Table 1 Comparison of the NO_2 sensing capability of the WO_3 nanoneedle film with those of previously reported WO_3-based NO_2 gas sensors.

WO_3 structure	NO_2 conc. ppmv	Response R_a/R_g	Sensor temp. °C	(response-1)/ NO_2 conc.	Ref.
WO_3 nanoneedle-assembled film	0.25	3.93	300	11.72	This study
	0.5	12.06	300	22.12	This study
	0.75	17.83	300	22.44	This study
	1	25.36	300	24.36	This study
	1.25	29.24	300	22.59	This study
		Limit of detection: 1.5 ppbv			
WO_3 particulate film	5	1.1	200	0.02	28
	10	1.6	200	0.06	
	100	20.36	200	0.19	
		Limit of detection: 5 ppmv			
WO_3 nanosheet-assembled microbrick	5	1.5	300	0.10	29
	10	2.5	300	0.15	
	100	11.5	300	0.11	
WO_3 polycrystalline film	1	1	250	0.00	30
	10	4	250	0.30	
	100	30	250	0.29	
Sprayed WO_3 thin film	10	1.2	200	0.02	31
	100	1.97	200	0.01	
		Detection limit: 10 ppmv			
WO_3 nanoflower	1	1.1	200	0.10	32
	5	1.2	200	0.04	
	10	1.45	200	0.05	
	20	2.05	200	0.05	
	40	2.15	200	0.03	
	60	3.00	200	0.03	
	80	3.10	200	0.03	
	100	3.23	200	0.02	
WO_3 nanoplate	5	1.36	150	0.07	33
	10	1.54	150	0.05	
	15	2.1	150	0.07	
	20	12.1	150	0.56	
Y-doped WO_3 nanoplate	5	3.7	150	0.54	
	10	21	150	2.00	
	15	88	150	5.80	
	20	101	150	5.00	
Bilayer polyaniline-WO_3 thin film	2	1.18	50	0.09	34
	4	1.23	50	0.06	
	6	1.45	50	0.08	
	8	1.66	50	0.08	
	10	2.39	50	0.14	
	20	14.47	50	0.67	
	30	60.9	50	2.00	
WO_3 nanorod	2	1.5	225	0.25	35
	5	1.8	225	0.16	
	10	2.12	225	0.11	
	20	2.65	225	0.08	
	50	3.55	225	0.05	

reactions. The adsorbed oxygen is consumed by the oxidation reaction. Electrons trapped in the adsorbed oxygen return to the particles, reducing the thickness of the electron depletion layer. The electrical resistance of the gas sensor decreases with increasing electrical conductivity between the particles. The sensing mechanism for the semiconductor gas sensor is the change in the electrical resistance of the particulate film owing to the oxidation reaction between the combustible gas and the adsorbed oxygen. The sensing mechanisms were reviewed in a previously published article[7].

The WO_3 nanoneedle film is very effective as a gas sensor because the nanoneedles were approximately 100 nm long and 10 nm wide and the electron depletion layer was several nanometers thick. Therefore, the entire nanoneedle became an electron-depletion layer. The electrical resistance of the electron-depletion layer was changed after oxidation of the combustible gas by the adsorbed oxygen; however, the electrical resistance inside the particles did not change, which is problematic for the detection of low gas concentrations. However, the electrical resistance of the nanoneedles changed drastically because almost all the nanoneedles became electron-depletion layers.

Furthermore, it is necessary to diffuse the gas over the entire sensitive film to detect low concentrations.

Table 2 Comparison of the acetone sensing capability of the WO_3 nanoneedle film with those of previously reported WO_3-based acetone gas sensors.

WO_3 structure	Acetone conc. ppmv	Response R_a/R_g	Sensor temp. °C	(response-1)/acetone conc.	Ref.
WO_3 nanoneedle-assembled film	0.025	1.049	300	1.96	This study
	0.05	1.218	300	4.36	This study
	0.075	1.491	300	6.55	This study
	0.1	2.043	300	10.43	This study
	0.125	2.392	300	11.14	This study
	0.25	3.591	300	10.36	This study
	0.5	5.713	300	9.43	This study
	0.75	6.777	300	7.70	This study
	1	7.418	300	6.42	This study
	1.25	7.656	300	5.32	This study
	10	19.72	300	1.87	This study
	Limit of detection: 2.4 ppbv				
WO_3 particulate film	100	18.51	200	0.18	36
Sea urchins-like WO_3	2	2.8	200	0.90	37
	5	4.7	200	0.74	
	10	6.4	200	0.54	
	100	27.2	200	0.26	
WO_3 nanosheet	100	12	340	0.11	
WO_3-C_3N_4 nanosheet	100	35	340	0.34	
5 mol% Cr_2O_3-doped WO_3 thin film	4.19	320		0.32	38
	15	6.13	320	0.34	
	20	8.91	320	0.40	
3 mol% Cu-doped WO_3 hollow fiber	6.43	300		0.27	39
Flower-like MoO_3/WO_3 (Mo:W = 4:1)	18.2	320		0.17	40
Flower-like WO_3	100	10.9	320	0.10	
Single crystalline WO_3 plate	15	307		0.14	42
	1000	105	307	0.10	
WO_3 particle	100	11	307	0.10	
	1000	27	307	0.03	
WO_3 hollow sphere	50	3.53	400	0.05	43
	100	4.56	400	0.04	
	200	6.04	400	0.03	
	500	13.5	400	0.03	
	1000	16	400	0.02	
	2000	18.6	400	0.01	
	5000	23.1	400	0.00	
WO_3 nanosheet	10	2.5	340	0.15	44
	20	4.5	340	0.18	

Table 2 continued

WO_3 structure	Acetone conc. ppmv	Response R_a/R_g	Sensor temp. °C	(response-1)/acetone conc.	Ref.
	50	7.5	340	0.13	
	100	9.5	340	0.09	
	300	13	340	0.04	
	500	14	340	0.03	
Ag QDs sensitized WO_3 nanosheet	2.5	340		0.15	
	20	5	340	0.20	
	50	8	340	0.14	
	100	12	340	0.11	
	300	17	340	0.05	
	500	19.5	340	0.04	

Therefore, porous thin films are effective in the detection of low gas concentrations. However, low-conductivity semiconductor particles increase the electrical resistance of the porous thin films. A large measuring instrument is needed to measure the high electrical resistance, which is problematic for miniature gas sensors. In contrast, nanoneedles have one-dimensional structures and exhibit high conductivities in the longitudinal direction of the particles. The highly conductive nanoneedles contribute to both the high porosity and conductivity. Therefore, nanoneedles are effective for detecting gases at low concentrations.

Notably, the WO_3 nanoneedle film sensor exhibited high responses to both NO_2 and acetone. NO_2 is an oxidizing and combustion-supporting gas. Combustion-supporting gases, such as NO_2, oxygen, air, chlorine, fluorine, and nitrogen monoxide, provide oxygen for combustion of combustible substances. Acetone is a reducing and combustible gas. Reducing gases such as acetone, H_2, carbon monoxide, hydrogen sulfide, and sulfur dioxide deplete oxygen. Combustible gases, such as acetone, H_2, methane, propane, and isobutane, burn in air or oxygen. The high responses to NO_2 and acetone, which have very different properties, is a significant characteristic of the WO_3 nanoneedles.

Moreover, the gas selectivities of metal-oxide gas sensors differ depending on the metal ions and their valences. Therefore, various metal oxide-based gas sensors have been developed. It is also known that different nanostructures present different gas selectivities because they exhibit different specific surface areas, crystal planes, and crystal defects. These features affect the gas selectivities and responses substantially, which has led to the development of various nanostructures for use in gas sensors. The high responses to both NO_2 and acetone is a major feature of the WO_3 nanoneedle film sensor, which distinguishes it from other materials. The metal type, metal valence, high specific surface area, crystal planes, and crystal defects contribute to the high responses to both NO_2 and acetone.

Conclusions

A highly responsive diabetes sensor was developed in which a WO_3 nanoneedle film was used to detect low concentrations of acetone gas. The WO_3 nanoneedle film was formed by heating an aqueous solution containing tungstic acid, CH_3CN, and HCl at 70 °C for 7 d. The WO_3 nanoneedle film was obtained by precisely controlling the crystallization process. The sensor exhibited a high sensor response of $R_a/R_g = 19.72$ to 10 ppmv acetone gas, demonstrating the ability to detect low concentrations of acetone. Furthermore, the sensor exhibited a high sensor response of $R_g/R_a = 25.36$ to 1 ppmv NO_2, which is a marker for asthma. The sensor responses to the lung cancer marker gases acetaldehyde and toluene were 13.54 and 9.49, respectively. The sensor responses to 10 ppmv isoprene, C_2H_5OH, para-xylene, H_2, and NH_3 were 7.93, 6.33, 4.51, 2.08, and 0.90, respectively. The WO_3 nanoneedle film sensor successfully detected 25 ppbv acetone and 250 ppbv NO_2. LODs of 2.4 and 1.5 ppbv were estimated for acetone and NO_2, respectively. This sensor detects low gas concentrations and is selective for acetone and NO_2. Biogases such as those in exhaled breath and skin gas are detected by the sensor, which will contribute to early screening of diabetes, asthma, and lung cancer.

Author contributions

Y.M. designed and directed the project. A.U. performed the measurements. Y.M. analyzed the data and wrote the article.

Conflict of interest

The authors declare no competing interests.

Received: 7 July 2023 Revised: 2 October 2023 Accepted: 20 October 2023.
Published online: 22 December 2023

References

1. Vasilescu, A., Hrinczenko, B., Swain, G. M. & Peteu, S. F. Exhaled breath biomarker sensing. *Biosens. Bioelectron.* **182**, 113193 (2021).
2. Wallace, M. A. G. & Pleil, J. D. Evolution of clinical and environmental health applications of exhaled breath research: Review of methods and instrumentation for gas-phase, condensate, and aerosols. *Anal. Chim. Acta* **1024**, 18–38 (2018).
3. Hakim, M. et al. Volatile Organic Compounds of Lung Cancer and Possible Biochemical Pathways. *Chem. Rev.* **112**, 5949–5966 (2012).
4. Baumbach, J. I. et al. Significant different volatile biomarker during bronchoscopic ion mobility spectrometry investigation of patients suffering lung carcinoma. *Int. J. Ion-. Mobil. Spectrom.* **14**, 159–166 (2011).
5. Yamane, N. et al. Relationship between skin acetone and blood β-hydroxybutyrate concentrations in diabetes. *Clin. Chim. Acta* **365**, 325–329 (2006).
6. Oh, Y. et al. Olfactory Detection of Toluene by Detection Rats for Potential Screening of Lung Cancer. *Sensors* **21**, 2967 (2021).
7. Masuda, Y. Recent advances in SnO_2 nanostructure based gas sensors. *Sens. Actuators B Chem.* **364**, 131876 (2022).
8. Masuda, Y. Ceramic nanostructures of SnO_2, TiO_2, and ZnO via aqueous crystal growth: cold crystallization and morphology control. *J. Ceram. Soc. Jpn.* **128**, 718–737 (2020).
9. Li, Y. et al. Formaldehyde detection: SnO2 microspheres for formaldehyde gas sensor with high sensitivity, fast response/recovery and good selectivity. *Sens. Actuators B Chem.* **238**, 264–273 (2017).
10. Suematsu, K. et al. Pulse-Driven Semiconductor Gas Sensors Toward ppt Level Toluene Detection. *Anal. Chem.* **90**, 11219–11223 (2018).
11. Pan, J., Ganesan, R., Shen, H. & Mathur, S. Plasma-Modified SnO2 Nanowires for Enhanced Gas Sensing. *J. Phys. Chem. C.* **114**, 8245–8250 (2010).
12. Kuang, X. et al. Hydrothermal synthesis of hierarchical SnO2 nanostructures made of superfine nanorods for smart gas sensor. *Appl. Surf. Sci.* **364**, 371–377 (2016).
13. Song, Y. G. et al. Ionic-Activated Chemiresistive Gas Sensors for Room-Temperature Operation. *Small* **15**, 1902065 (2019).
14. D'Arsié, L. et al. Improved recovery time and sensitivity to H2 and NH3 at room temperature with SnOx vertical nanopillars on ITO. *Sci. Rep.* **8**, 10028 (2018).
15. Kim, K. et al. Synergistic approach to simultaneously improve response and humidity-independence of metal-oxide gas sensors. *J. Hazard. Mater.* **424**, 127524 (2022).
16. Van Dang, T., Duc Hoa, N., Van Duy, N. & Van Hieu, N. Chlorine Gas Sensing Performance of On-Chip Grown ZnO, WO3, and SnO2 Nanowire Sensors. *ACS Appl. Mater. Interfaces* **8**, 4828–4837 (2016).
17. Tang, H. et al. Room temperature ppt-level NO_2 gas sensor based on SnO_x/SnS nanostructures with rich oxygen vacancies. *2D Mater.* **8**, 045006 (2021).
18. Masuda, Y. Facet controlled growth mechanism of SnO_2 (101) nanosheet assembled film via cold crystallization. *Sci. Rep.* **11**, 11304 (2021).
19. Masuda, Y., Itoh, T., Shin, W. & Kato, K. SnO_2 Nanosheet/Nanoparticle Detector for the Sensing of 1-Nonanal Gas Produced by Lung Cancer. *Sci. Rep.* **5**, 10122 (2015).
20. Masuda, Y., Kato, K., Kida, M. & Otsuka, J. Selective nonanal molecular recognition with SnO_2 nanosheets for lung cancer sensor. *Int. J. Appl. Ceram. Technol.* **16**, 1807–1811 (2019).
21. Kim, K., Choi, P. G., Itoh, T. & Masuda, Y. Catalyst-free Highly Sensitive SnO_2 Nanosheet Gas Sensors for Parts per Billion-Level Detection of Acetone. *ACS Appl. Mater. Interfaces* **12**, 51637–51644 (2020).
22. Choi, P. G., Izu, N., Shirahata, N. & Masuda, Y. Improvement of sensing properties for SnO_2 gas sensor by tuning of exposed crystal face. *Sens. Actuators B Chem.* **296**, 126655 (2019).
23. Choi, P. G., Izu, N., Shirahata, N. & Masuda, Y. SnO_2 Nanosheets for Selective Alkene Gas Sensing. *ACS Appl. Nano Mater.* **2**, 1820–1827 (2019).
24. Li, C., Choi, P. G. & Masuda, Y. Highly Sensitive and Selective Gas Sensors Based on NiO/MnO2@NiO Nanosheets to Detect Allyl Mercaptan Gas Released by Humans under Psychological Stress. *Adv. Sci.* https://doi.org/10.1002/advs.202202442 (2022).
25. Choi, P. G. & Masuda, Y. Nanosheet-type tin oxide gas sensor array for mental stress monitoring. *Sci. Rep.* **12**, 13874 (2022).
26. Kim, K., Choi, P. G., Itoh, T. & Masuda, Y. Atomic step formation on porous ZnO nanobelts: remarkable promotion of acetone gas detection up to the parts per trillion level. *J. Mater. Chem. A* **10**, 13839–13847 (2022).
27. Kim, K., Choi, P. G., Itoh, T. & Masuda, Y. Effect of Coordinatively Unsaturated Sites in MOF-Derived Highly Porous CuO for Catalyst-Free ppb-Level Gas Sensors. *Adv. Mater. Interfaces* **8**, 2100283 (2021).
28. Kamble, C. & Panse, M. IDE embedded tungsten trioxide gas sensor for sensitive NO2 detection. *Mater. Chem. Phys.* **224**, 257–263 (2019).
29. Harale, N. S. et al. Single-step hydrothermally grown nanosheet-assembled tungsten oxide thin films for sensitive and selective NO2 gas detection. *J. Mater. Sci.* **53**, 6094–6105 (2018).
30. Siciliano, T. et al. WO3 gas sensors prepared by thermal oxidization of tungsten. *Sens. Actuators B: Chem.* **133**, 321–326 (2008).
31. Ganbavle, V. V., Mohite, S. V., Agawane, G. L., Kim, J. H. & Rajpure, K. Y. Nitrogen dioxide sensing properties of sprayed tungsten oxide thin film sensor: Effect of film thickness. *J. Colloid Interface Sci.* **451**, 245–254 (2015).
32. Hingangavkar, G. M., Navale, Y. H., Nimbalkar, T. M., Mulik, R. N. & Patil, V. B. Hydrothermally engineered WO3 nanoflowers: A selective detection towards toxic NO2 gas. *Sens. Actuators B: Chem.* **371**, 132584 (2022).
33. Mathankumar, G. et al. Defect manipulation of WO3 nanostructures by yttrium for ultra-sensitive and highly selective NO2 detection. *Sens. Actuators B: Chem.* **353**, 131057 (2022).
34. He, W., Zhao, Y. & Xiong, Y. Bilayer Polyaniline–WO3 Thin-Film Sensors Sensitive to NO2. *ACS Omega* **5**, 9744–9751 (2020).
35. Behera, B. & Chandra, S. Synthesis of WO3 nanorods by thermal oxidation technique for NO2 gas sensing application. *Mater. Sci. Semicond. Process* **86**, 79–84 (2018).
36. Wang, Q. et al. Sea urchins-like WO3 as a material for resistive acetone gas sensors. *Sens. Actuators B: Chem.* **355**, 131262 (2022).
37. Wang, D. et al. Ultrathin WO3 nanosheets modified by g-C3N4 for highly efficient acetone vapor detection. *Sens. Actuators B: Chem.* **282**, 961–971 (2019).
38. Gao, P., Ji, H., Zhou, Y. & Li, X. Selective acetone gas sensors using porous WO3–Cr2O3 thin films prepared by sol–gel method. *Thin Solid Films* **520**, 3100–3106 (2012).
39. Bai, X., Ji, H., Gao, P., Zhang, Y. & Sun, X. Morphology, phase structure and acetone sensitive properties of copper-doped tungsten oxide sensors. *Sens. Actuators B: Chem.* **193**, 100–106 (2014).
40. Sun, Y. et al. Synthesis of MoO3/WO3 composite nanostructures for highly sensitive ethanol and acetone detection. *J. Mater. Sci.* **52**, 1561–1572 (2017).
41. Wang, Y.-d, Ma, C.-l, Sun, X.-d & Li, H.-d Preparation of nanocrystalline metal oxide powders with the surfactant-mediated method. *Inorg. Chem. Commun.* **5**, 751–755 (2002).
42. Liu, S., Zhang, F., Li, H., Chen, T. & Wang, Y. Acetone detection properties of single crystalline tungsten oxide plates synthesized by hydrothermal method using cetyltrimethyl ammonium bromide supermolecular template. *Sens. Actuators B: Chem.* **162**, 259–268 (2012).
43. Li, X.-L., Lou, T.-J., Sun, X.-M. & Li, Y.-D. Highly Sensitive WO3 Hollow-Sphere Gas Sensors. *Inorg. Chem.* **43**, 5442–5449 (2004).
44. Yin, M., Yu, L. & Liu, S. Synthesis of Ag quantum dots sensitized WO3 nanosheets and their enhanced acetone sensing properties. *Mater. Lett.* **186**, 66–69 (2017).
45. Analytical Methods, C. Recommendations for the definition, estimation and use of the detection limit. *Analyst* **112**, 199–204, (1987).